GEM-TN-92-125

Alignment Requirements for the GEM Muon Detector

J. Paradiso
C.S. Draper Laboratory

June 1992

Abstract

A table of requirements is derived for local and global alignment of the GEM muon detector. Requirements are given for structural accuracy (to which the muon array must be constructed) and precision measurement (where dynamic measurements of detector position may be used to compensate the location of superlayer spacepoints). In order to facilitate the rapid updating of requirements as the detector definition evolves, details are given on the requirement derivation.

Alignment Requirements for the GEM Muon Detector

--J. Paradiso, June '92

1) Introduction

Several phenomena that impact muon system alignment are listed below:

Intrinsic Smears

• Vertex distribution along z
• Multiple scattering in calorimeter

Needed Structural Accuracy

• Dynamic range of local alignment system
• Alignment of trigger roads

Precision Measurements

• Stated momentum precision in bending plane
• Align to precision of detector components (muon angle)
• Extrapolate $p_{\parallel}$ from measured angle
• Mass Resolution

Pattern Recognition

• Muon tracking constraints
• Track linking with central detector

Other Effects

• Line-of-sight deviation from IP

The "intrinsic smears" arising from the vertex spread along the beamline and multiple scattering in the calorimeter can limit the required alignment accuracy in some coordinates. The accuracy of the structure itself (after it is servoed into position) is driven by the dynamic range of the straightness monitor system (used for local alignment), and the trigger road definition/width. The precision measurements set the needed accuracy of the alignment monitors (which will be used to correct the muon data). The major influence here is the muon $p_{\perp}$ measurement. Some quantities will require determination of the muon angle; the needed resolutions are quoted here. Pattern recognition considerations may also affect some of these requirements, and track linking with the central detector will induce a limit on the angular error (such effects are not included in this report). Other considerations, such as the sensitivity to torque error in a straight-line alignment system pointing back toward the interaction point, are analyzed.

Figs. 1-4 show simplified views of the GEM muon system, with relevant quantities labeled. Local coordinate offsets are given, plus a net translation of the hexant coordinate system (Δx_G, Δy_G, Δz_G). The angular errors ($\Delta\theta$, $\Delta\phi$) arise from a rotation of the hexant about the IP before translation. Various quantities are assumed in these

derivations; these are listed where relevant, hence may be readily updated, and the results normalized accordingly. The simplified muon system depicted in this analysis has a barrel running from $\theta = 90° \rightarrow 30°$, and an endcap running from $\theta = 30° \rightarrow 10°$.

2) Intrinsic Smears

a) Length of interaction diamond

Assuming the interaction diamond to be of length $\sigma = 7$ cm along the z-axis, we generate a probable error along the beam axis of $\Delta z_G = \pm 4.7$ cm. This error is only relevant to the static structure requirements (in Sec. 3); on an event-by-event basis, the vertex position is measured by the central tracker, hence this is corrected. Since this variation is only an offset along the z-axis, the perceived θ angle is unchanged. The θ accuracy of the structure (which assumes that all muons originate at the IP), however, is smeared by this distribution. In the barrel, the effective shift in θ may be parameterized by $\Delta\theta \approx (D \sin^2\theta_\mu / y_c)$, where $D = \pm 4.7$ cm, and $y_c = 8.53$ m (for the outer RPC layer). This gives $\Delta\theta = \pm 5.5$ mr @ $\theta = 90°$, and $\Delta\theta = \pm 1.4$ mr @ $\theta = 30°$. For the endcap, this relation may be adapted; $\Delta\theta \approx (D \sin\theta_\mu \cos\theta_\mu / z_c)$, where $z_c = 16$ meters. This yields the results: $\Delta\theta = \pm 1.4$ mr @ $\theta = 30°$, and $\Delta\theta = \pm 0.5$ mr @ $\theta = 10°$. Because of the projective geometry of the barrel and endcap structure, an effective smear in the y axis may also be inferred (mainly relevant when specifying the alignment of trigger elements). This parameterizes as $\Delta y_G = \Delta z_G \tan\theta$, and evaluates to $\Delta y_G = \pm\infty$ @ $\theta = 0°$, $\Delta y_G = \pm 2.7$ cm @ $\theta = 30°$, and $\Delta y_G = \pm 8.3$ mm @ $\theta = 10°$. Since the beam diameter is very small (i.e. on the order of 10 μm), there is no significant primary smear generated in the radial axes.

b) Multiple Scattering

Another smear contributing to the global alignment accuracy is due to multiple scattering of muons in the calorimeter. Assuming a 2.5 meter long copper calorimeter (175 radiation lengths), and $\alpha_{ms} = (.015/P(GeV))\sqrt{\ell/\ell_0}$ (FWHM) , we calculate $\alpha_{ms} = 0.4$ mr at 500 GeV momentum (4.0 mr at 50 GeV). Assuming a maximum momentum of interest to be 500 GeV (these figures can be scaled for other momenta), this error translates directly into polar angle and azimuth: $\Delta\theta, \Delta\phi = \pm 0.2$ mr. Projecting onto the barrel yields: $\Delta z = (r\,\Delta\theta)/\sin\theta$, $\Delta y = (r\,\Delta\theta)/\cos\theta$, $\Delta x = (r\,\Delta\theta)$, where the radius "r" is evaluated at the first chamber layer (since we are projecting back to the IP); $r = y_a/\sin\theta$. For the endcap, we have: $\Delta y = (r\,\Delta\theta)/\cos\theta$, $\Delta z = (r\,\Delta\theta)/\sin\theta$, $\Delta x = (r\,\Delta\phi)$, where r is now

defined along z; $r = z_a/\cos\theta$. Plugging in $y_a = 3.9$ m, $z_a = 6.3$ m, we get (for the barrel): ($\Delta z_G = \pm\infty$, $\Delta y_G = \pm 780$ μm, $\Delta x_G = \pm 780$ μm) at $\theta = 90°$, ($\Delta z_G = \pm 1.6$ mm, $\Delta y_G = \pm 900$ μm, $\Delta x_G = \pm 780$ μm) at $\theta = 30°$, and (for the endcap): ($\Delta z_G = \pm 2.5$ mm, $\Delta y_G = \pm 1.5$ mm, $\Delta x_G = \pm 1.3$ mm) at $\theta = 30°$, ($\Delta z_G = \pm 7.3$ mm, $\Delta y_G = \pm 1.3$ mm, $\Delta x_G = \pm 1.3$ mm) at $\theta = 10°$. For scattering at 50 GeV (the highest energy cut considered for the muon trigger), these factors may be scaled up by an order of magnitude.

3) Structural Accuracy

a) Dynamic range of local alignment systems

It is vital that the structure be designed such that its relative deflection will be within range of the local alignment systems and straightness monitors. In deriving these numbers, a series of assumptions must be taken. The LED/lens straightness monitors currently have a measurement range that (in the best case) is within ±1 mm, and a capture range (with a saturated measurement that indicates the offset direction) of ±3 mm, within which the chamber layers may be servoed into measurement position. After some development, these limits may be extended; i.e. by imaging a wide square on a large quadrant diode (or by using an imaging array), a dynamic range approaching ±5 mm may be attained for the precision measurement. In the current analysis, the conservative estimate of ±1 mm is used (this is also compatible with the present range of measurement obtained from stretched wire techniques). Bear in mind that a servo system or sensor range extension will increase these numbers (which can be scaled accordingly).

For the barrel (Fig. 5), the local x-axis positioning is set directly by the range of the z-axis multipoint and inter-superlayer monitors, thus we derive $\Delta x < \pm 1$ mm (the situation is actually slightly more complicated; the maximum x-axis deviation from a line along the z-axis connecting the chamber packages in a superlayer is ±1 mm, while for a line connecting outer and inner superlayers [fixed at the inner superlayer], the middle superlayer offset is required to be within ±1 mm, yet the outer superlayer can be displaced by ±2 mm [this comes from the requirement of "straightness" along the muon path]). Within a superlayer, the y offset between chamber packages must be within $\Delta y <$ ±1 mm, in order to maintain the range constraint on the z-axis multipoint monitors. Between superlayers, however, the alignment path at $\theta = 30°$ applies the worst-case constraint (since the sensors are angled to be orthogonal to a ray inclined at $\theta = 30°$, $\phi = 11.25°$), namely: $\Delta y_b < \pm(1\text{ mm})\cos 30° = \pm 870$ μm (at $\theta = 90°$, this measurement is limited by the $\Delta\phi$ of a hexant, i.e. $\Delta y_b < \pm(1\text{ mm})\cos 11.25°/\tan 11.25° = 4.9$ mm). The

z offset error is determined by the inter-superlayer monitors; i.e. $\Delta z_b < \pm$ 1 mm @ $\theta = 90°$, and $\Delta z_b < \pm$(1 mm) cos 30°/tan 30° = ±1.5 mm @ $\theta = 30°$. For the inter-superlayer monitors, if the measurement is referenced to the inner layer, the upper layer tolerances (Δy_c, Δz_c) are twice the (Δy_b, Δz_b) values (this is only true for the subscripted quantities; the Δy measured by the multipoint monitors along the z-axis must all be within ±1 mm to stay in range).

For the endcap (Fig. 6), all monitors are considered to be of the 3-point inter-superlayer variety. As above, the measurements are assumed to be referenced to the inner layer; the numbers quoted here are thus relevant for the middle superlayer, and can be doubled for the outer superlayer. Translations along the x & y axes are directly measured (as the sensors are not inclined in these coordinates, and are orthogonal to the z-axis), thus $\Delta x_b < \pm 1$ mm, $\Delta y_b < \pm 1$ mm. Translations along z will project across the sensor, yielding: $\Delta z_b <$ ±(1 mm)/tan θ, thus $\Delta z_b < 1.7$ mm @ $\theta = 30°$ and $\Delta z_b < 5.7$ mm @ $\theta = 10°$.

b) Projective Constraints for the Trigger

The other factor influencing the structural accuracy is the alignment of projective strips for the trigger system. In this analysis, a misalignment of trigger strips was tolerated that caused a loss of up to 10% in projective coincidence (as this loss factor is somewhat arbitrary, it may eventually prove desirable to scale these results to a different figure-of-merit). This analysis does not include effects of z-vertex smearing from the interaction diamond or multiple scattering (which will nonetheless have considerable impact; the effect on chamber alignment from each process is identified separately, and compared in the conclusion of this report). In the measured non-bending coordinates (z in the barrel, y in the endcap), coincidences are required to be of single-strip width, while in the bending coordinate (x in the barrel and endcap), candidate muons are required to have their hits contained in a cone (defined from inner to outer superlayer) of 1° (barrel) or .45° (endcap). This constraint was vaguely derived from the various trigger schemes that are proposed for muons over 50 GeV. This purpose of this analysis is to derive a feel for the alignment requirements for the trigger; it should be updated in a more precise fashion as the trigger definition improves.

Measuring the z-coordinate of the barrel, pickup strips run in the local x-direction (Fig. 2) and are sized projectively, measuring 8.9 cm (at $y_c = 8.53$ cm), 6.5 cm (at $y_c =$ 6.08 cm), and 3.9 cm (at $y_c = 4.15$ cm). The nominal angular pitch of these strips is thus $\Delta\theta = 0.6°$. Referencing the coordinates to the inner layer, a 10% loss results when

moving the middle layer by $\Delta z_b = \pm 3.25$ mm or the outer layer by $\Delta z_c = \pm 4.5$ mm. The relative scale of the strip pitch changes when the chamber layers are displaced radially (Δh in Figs. 1 & 2) as: $\Delta z = \Delta h / \tan\theta$. This gives essentially infinite tolerance to Δh at $\theta = 90°$, but produces an effect at smaller angle; at $\theta = 30°$, a $\Delta y_b = \pm 1.9$ mm or a $\Delta y_c = \pm 2.6$ mm will produce a 10% loss in projective overlap between the inner and middle strips.

The x-measuring strips are sized at 1.3 cm in the barrel (this sizing is specified identically for all layers, hence they are essentially non-projective). Assuming that a trigger architecture maps three strips on the middle layer) to 5 strips on the outer layer, the effective middle strip width is 3.9 cm, and the outer strip width is 6.5 cm. The 10% criterion will thus yield allowable bending offsets of $\Delta x_b = \pm 2$ mm for the middle layer and $\Delta x_c = \pm 3.25$ mm for the outer layer. Translating these into Δh errors at the edges of the hexant (i.e. $\Delta x = \Delta h / \tan 11.25°$ as was performed above), yields $\Delta y_b = \pm 1.0$ cm and $\Delta y_c = \pm 1.6$ cm, both fairly loose tolerances.

Looking at the global requirements for the barrel trigger in rϕ, we see that an x-translation of the IP (by Δx_G) relative to the hexant centerline (see Fig. 2) will create an angle of $\Delta x_G / y_c$ at the outer chamber layer. If we translate this back to the inner chamber layer, we derive an offset of $\Delta x_a = (y_c - y_a)\ \Delta x_G / y_c$. Using the 10% criterion, we require this shift to lose under 10% net projection, thus (referencing the outer strip width), $\Delta x_a < \pm 3.25$ mm, hence $\Delta x_G < \pm 6.3$ mm. Moving the hexant away from the IP along the local radial axis (y in Fig. 2) changes the aspect of the hexant edges (i.e. the ϕ angles spanned by the inner and outer superlayers relative to the IP are no longer equal [at 22.5°]). This shift (difference in angle to IP from ends of outer and inner superlayers) causes a projective loss at the hexant edges for muons coming from the IP, estimated as $\Delta x = \tan 11.25° (y_c - y_a [y_c + \Delta y]/[y_a + \Delta y])$. Simplifying and rearranging (assuming Δx small with respect to y_a) yields $\Delta y_G = \Delta x/(\tan 11.25° [(y_c/y_a) - 1])$. If we assume our Δx to be the ± 3.25 mm derived from the 10% loss criterion (which may be overly restrictive here), we derive $\Delta y_G = \pm 1.5$ cm; again, a liberal margin.

A similar set of global constraints can be determined for the barrel in rθ. Translating a barrel hexant by Δz_G produces a projective loss at the outermost layer of $\Delta z_G [(y_c/y_a) - 1]$. As y_c is nearly twice y_a, the quantity in brackets approaches unity. Using the 10% loss criterion for Δz_c developed above, we derive $\Delta z_G \approx \Delta z_c = \pm 4.5$ mm. The effect of a radial (i.e. Δy) hexant shift can be determined by the same formula as used for rϕ, which now becomes: $\Delta z = \cot\theta\ (y_c - y_a [y_c + \Delta y]/[y_a + \Delta y])$, and can be rearranged into: $\Delta y_G = \Delta z/(\cot\theta [(y_c/y_a) - 1])$. If we plug in the familiar $\Delta z_c = \pm 4.5$ mm

from the 10% criteria (again, probably conservative), we get a worst-case $\Delta y_G = \pm 2.5$ mm at $\theta = 30°$.

The nonbending coordinate measured by the endcap lies along the local y axis (see Figs. 3 & 4). This is measured by groups of anode wires that span a 5 cm interval (since the chambers within a superlayer are offset by half of this distance, the effective y granularity is divided by ÷2, yielding roughly a 3.5 cm span). If one desires to form a nonbending trigger in the endcap, the y measurements (which don't necessarily line up projectively between superlayers!) must be aligned. If one assumes the 10% loss criterion here, mapping one middle-layer strip to two outer-layer strips (to become vaguely projective), we develop a tolerance of $\Delta y_b = \pm 1.75$ mm, $\Delta y_c = \pm 3.5$ mm. This can also be extended to the Δh between layers, which now lies along the z axis. The major restriction is at $\theta = 30°$, which yields $\Delta z_b = (\pm 1.75 \text{ mm})/\tan 30° = \pm 3.0$ mm, $\Delta z_c = \pm 6.0$ mm.

The bending coordinate is measured by radially-directed 5 mm strips. To become efficient beyond 50 GeV, a trigger coincidence maps a hit in the middle layer to a range of ±6.5 strips, as extrapolated at the outer layer. Making this a bit more conservative & arbitrary (as we did in the barrel), we assume that we map a hit in the inner layer to a ±2 cm range in the middle layer and a ±3.25 cm range in the outer layer, from which we derive requirements of $\Delta x_b = \pm 2$ mm and $\Delta x_c = \pm 3.25$ mm. Extrapolating this to a Δh constraint, we get a worst-case $\Delta h = \Delta x/(\sin 30° \tan 11.25°)$, which produces $\Delta z_b = \pm 2.0$ cm and $\Delta z_c = \pm 3.3$ cm; certainly loose requirements.

Applying the same relation as used in the barrel, the $r\phi$ projection gives a constraint on Δx_G; i.e. $\Delta x_a = (z_c - z_a) \ \Delta x_G/z_c$. Plugging in $\Delta x_a = \pm 3.25$ mm gives $\Delta x_G = \pm 5.6$ mm. A limit on Δz_G can also be estimated from projective loss, as was seen in the barrel: $\Delta z_G = \Delta x/(\tan\theta\,[(z_c/z_a)-1])$. Setting $\Delta x = \pm 3.25$ mm, we get $\Delta z_G = \pm 4.1$ mm @ $\theta = 30°$, and $\Delta z_G = \pm 1.4$ cm @ $\theta = 10°$.

Adapting the $r\theta$ formulae developed for the barrel, we can calculate the projective loss resulting from a global y translation: $\Delta y\,[(z_c/z_a) - 1]$. Requiring this to remain under 10% (and plugging in $\Delta y = \Delta y_c = \pm 3.5$ mm) gives $\Delta y_G = \pm 4.8$ mm, which results in a z requirement of $\Delta z_G = \pm 4.4$ mm @ $\theta = 30°$ and $\Delta z_G = \pm 15$ mm @ $\theta = 10°$.

Since our angles $\Delta\theta$ and $\Delta\phi$ are defined to be rotations about the IP (before applying the global coordinate translations), the trigger is essentially invariant to them; i.e. all stiff tracks will still be projective to the IP. Because a narrow (1 or 2 strip) road was employed in the nonbending trigger definition (which may not be necessary), the nonbending requirements have become more stringent than the requirements in the bending plane; depending on how the trigger is actually defined, this may not be valid,

and the nonbending position tolerances may be appreciably liberalized. Again, this analysis is admittedly based on somewhat crude assumptions, and should eventually be updated with a better-defined trigger scenario.

4) Precision Measurements

a) Stated momentum resolution in bending plane

The figures summarized in this section are the alignment accuracies required to produce the stated momentum resolution i.e. $\Delta p/p$ = 5% (η = 0), 10% (η = 2.5). The muon detector structure need not produce this precision; rather the alignment system will resolve a set of corrections to the chamber positioning for off-line analysis.

The local positioning requirements (within a hexant) are quite exacting. First consider the barrel. In the bending coordinate (referencing measurements to the lower layer), we have the classic figures: $\Delta x_b = \pm 25$ μm and $\Delta x_c = \pm 50$ μm (the doubling of this figure at the outer layer is derived from the nature of this requirement; i.e. deviation of the chamber fiducials from a straight line). This also gives rise to a corresponding Δh requirement at the ϕ extremes of the hexants ($\phi = \pm 11.25°$): $\Delta x = \Delta h \tan 11.25°$. The full ±25 μm error budget is blown if Δy_b exceeds ±125 μm or Δy_c grows beyond ±250 μm. This error is a function of $\tan(\Delta\phi)$, and decreases nearly linearly to zero at the centerline of the hexant. As the subtended angle is small, the tangent is nearly linear, and the mean is readily taken (giving half of the maximum value). Thus, keeping the average contributed error from Δh a factor of 4 below the ±25 μm Δx error in the quadrature sum will result in a Δh limit of: $\Delta y_b = \pm 63$ μm and $\Delta y_c = \pm 125$ μm.

The situation is analogous in the endcaps, where again, Δx_b = 25 μm & Δx_c = 50 μm. The Δh situation is now slightly different; since the endcap chambers are projective to the beam axis, and the lines from the IP to the hexant edges approach the polar (z) axis, the effective $\Delta\phi$ angle is smaller. The sagitta effect becomes: $\Delta x = \Delta h \sin\theta \tan 11.25°$. Plugging in the 25 micron maximum, we blow our budget at $\Delta y_b = \pm 250$ μm ($\theta = 30°$) and $\Delta y_c = \pm 720$ μm ($\theta = 10°$). Again, doing approximate averaging, and keeping the Δh error a factor of 4 lower than the 25 micron maximum Δx contribution yields the tolerances: $\Delta y_b = \pm 125$ μm, $\Delta y_c = \pm 250$ μm ($\theta = 30°$), & $\Delta y_b = \pm 360$ μm, $\Delta y_c = \pm 720$ μm ($\theta = 10°$).

Shifts in the local z axis have no significant effect on the precision momentum measurement. Local Δh shifts also affect the point along the particle path where the

measurement is assumed to be taken, but this error is comparatively insignificant (for a 5% momentum resolution, this Δh position requirement is at least ± 10 cm).

The precision momentum requirements are a function of relative superlayer displacement, and nominally do not involve global alignment. One caveat, however, is a desire to know the position of the beamline relative to the muon array in the $r\phi$ plane, which increases the effective lever arm, thus provides enhanced momentum resolution for very high energy muons (circa 500 GeV and beyond) that scatter less in the calorimeter. This translates into a Δx_G constraint (see Fig. 2); i.e. $\Delta x_G = \pm 200$ μm. Physically, this may be interpreted as the desire to point the axes of the straightness monitors at the IP (in $r\phi$) to within 200 μm (this imposes no $\Delta\phi$ constraint, as ϕ is defined in Fig. 2). If one looks at the requirement of $\Delta x_G = \pm 200$ μm as an angular constraint on the straightness monitor axes (as measured at the outer superlayer), we have pointing needs of $\beta = 23$ μr @ $\theta = 90°$, $\beta = 12$ μr @ $\theta = 30°$ [worst case!]. This parameter is interpreted more as a "goal" than a requirement; i.e. it's not needed to meet the muon detector specifications, but would be a nice extrapolation.

b) Aligning to the ultimate measurement precision

There is no need to specify requirements on global alignment that are significantly more stringent than the possible measurement accuracy of the detector. Figs. 7 & 8 show calculations[1] of the detector resolution in x,z,θ,ϕ, which were made by fitting a muon track through the 3 superlayers (using the quoted resolution), and extrapolating back to the IP. These results include multiple scattering in the calorimeter, giving rise to a family of curves, as shown. The ultimate precision possible occurs at high energy (i.e. beyond 250 GeV for the z coordinate and above 2 TeV for the bending coordinate). Reading off these plots (and normalizing from σ to half-width), we obtain best-case resolutions for the barrel of $\Delta x_G = \pm 330$ μm, $\Delta z_G = \pm 1.3$ cm, $\Delta\theta = \pm 2.7$ mr ($\theta = 90°$), $\Delta\theta = \pm 0.67$ mr ($\theta = 30°$), $\Delta\phi = \pm 0.13$ mr. Doing the same for the endcap, we get: $\Delta x_G = \pm 330$ μm ($\theta = 30°$), $\Delta x_G = \pm 130$ μm ($\theta = 10°$), $\Delta z_G = \pm 1.5$ cm ($\theta = 30°$), $\Delta z_G = \pm 5.3$ cm ($\theta = 10°$), $\Delta\theta = \pm 2.7$ mr, $\Delta\phi = \pm 1.3$ mr. Using the Δz_G or $\Delta\theta$ resolutions, a limit for Δy_G may be estimated. Employing the former technique on the barrel, $\Delta y_G = \Delta z_G \tan\theta$, resulting in the most restrictive limit at $\theta = 30°$, where $\Delta y_G = \pm 1.6$ mm. Doing this to the endcap, we see $\Delta y_G = \pm 9$ mm, essentially independent of θ.

c) Projecting the total momentum

One of the major precision requirements on the polar muon angle (θ) accuracy is generated by the projection from the measured transverse momentum to the total muon momentum:

$$p = \frac{p_\perp}{\sin\theta}$$

Performing a tangent error analysis on this relation yields:

$$\frac{\sigma_p}{p} = \sqrt{\left(\frac{\sigma_{p_\perp}}{p_\perp}\right)^2 + \left(\sigma_\theta \cot\theta\right)^2} \qquad (\sigma_\theta \text{ in radians})$$

As a rule of thumb, we decide to keep ($\sigma_\theta \cot\theta$) a factor of four below $\sigma_{p_\perp}/p_\perp$, in order that angle error will contribute below 10% to the quadrature error sum. As θ approaches 90°, the muon momentum is totally transverse, hence σ_p is not sensitive to angle error. At $\theta = 30°$, however, we calculate the limit: $\sigma_\theta < 10$ mr [$\Delta\theta = \pm 6.7$ mr] (assuming $\sigma_{p_\perp}/p_\perp = 7\%$, as calculated at $p_\perp = 500$ GeV), and at $\theta = 10°$, we see that $\sigma_\theta < \pm 4.4$ mr [$\Delta\theta = \pm 2.9$ mr] (assuming $\sigma_{p_\perp}/p_\perp = 7\%$, as quoted).

Using the geometry of the muon array, y_G and z_G tolerances can be inferred from this θ resolution (the projections were given in Sec. 2b on multiple scattering); the position of the innermost chamber layer is taken as the lever arm (producing the tightest requirements). At $\theta = 30°$, we get ($\Delta z = \pm 10$ cm, $\Delta y = \pm 6.0$ cm), and at $\theta = 10°$, we see ($\Delta z = \pm 10$ cm, $\Delta y = \pm 2$ cm); certainly loose requirements!

d) Invariant Mass Resolution

The invariant mass of a muon pair is a function of the 3-momenta and opening angle:

$$m^2 = 4\, p_1\, p_2 \sin^2\left(\tfrac{1}{2}\theta_{\mu\mu}\right)$$

Performing a tangent error analysis will yield:

$$\frac{\sigma_m}{m} = \sqrt{2\left(\frac{\sigma_p}{p}\right)^2 + \left[\sigma_{\mu\mu} \cot\left(\tfrac{1}{2}\theta_{\mu\mu}\right)\right]^2} \qquad (\theta_{\mu\mu} \text{ in radians})$$

At this point, a series of assumptions must be made. First, as above, it is assumed that the angle error term will be a factor of four below the σ_p/p term, in order to achieve under 10% impact in quadrature. Next we assume σ_p/p to be at its quoted best (i.e. 5%). Finally, we must make assumptions about the opening angle. Nominally these will be set from decay kinematics, but we can make a few simplifications. For large angle, with muons nearly back-to-back, the angle error has no impact on the mass resolution. For small angle pairs, the angular term can dominate; however when the angle is below 22.5° (the ϕ span of a hexant), it becomes increasingly probably that both muons will stay within one hexant, thus the global alignment of hexant-to-IP will be of no consequence. The worst-case assumption (i.e. smallest opening angle) adopted here is thus $\theta_{\mu\mu}$ = 11.25°.

Plugging these assumptions into the above relations will yield: $\sigma_{\mu\mu}$ = 2.5 mr. Since we define $\theta_{\mu\mu}$ to be the difference between measured muon angles, the allowed error in each muon angle will be smaller by a factor of ÷2. Assuming the errors in θ and ϕ to be equal (which may need some qualification...), we obtain $\sigma_\theta = \sigma_\phi$ = 1.8 mr, hence $\Delta\theta = \Delta\phi = \pm 1.2$ mr.

Once more, we can apply geometrical projections to estimate equivalent errors induced in the global axes, employing the assumptions (i.e. referencing to the inner layer) & relations explained in the previous section. This yields ($\Delta x_G = \pm 4.7$ mm, $\Delta z_G = \pm 4.7$ mm) @ θ = 90°, ($\Delta x_G = \pm 9.4$ mm, $\Delta y_G = \pm 1.1$ cm, $\Delta z_G = \pm 1.9$ cm) @ θ = 30°, ($\Delta x_G = \pm 7.2$ mm, $\Delta y_G = \pm 8.4$ mm, $\Delta z_G = \pm 4.8$ cm) @ θ = 10°.

Again, the assumptions implicit in this analysis are somewhat rudimentary, and could stand refining.

5) Pattern Recognition

a) Muon Tracking Constraints

No analysis of pattern recognition requirements has been attempted here for tracking in the muon system. Because of the low rate in the barrel, one would assume that pattern ambiguities would be fairly minimal, excepting difficulties from punch-through hadrons, secondary particles exiting the calorimeter together with a muon, and random neutron background. At small θ, the rate is considerably higher, thus pattern matching considerations may begin to impact the alignment needs. A positioning accuracy of Δx, Δy, Δz on the order of ±1 mm has been discussed in this context, but no supporting analysis has been presented, thus more work is necessary at this point.

b) Track Linking with Central Detector

A neat solution to measuring a precise muon angle is to find the muon track in the central tracker, where it is determined very exactly. In order to accomplish this, one must match a track in the central region (complete with its associated clutter) to a companion seen in the muon detector. One can thus define a fiducial angle around a muon track that determines a cone, within which a match is searched for in the inner tracker. The angle subtended by this cone would provide another driver to the muon alignment accuracy. At this point, no such analysis exists; the best one can ask for, however, is to have the muon system aligned to the limit expected from multiple scattering in the calorimeter, which was discussed in Sec. 2b.

6) Other Effects

a) Line-of-sight deviation from the IP

The alignment accuracies that are quoted can (in some sense) be a function of the type of alignment system that is actually adopted. The baselined GEM alignment scheme (Figs. 5,6) assumes L3-type straightness monitors[2] to measure the bend-plane misalignment between muon superlayers. If these straightness monitor lines-of-sight (LOS) are all projectively oriented toward the IP, "torque error" (in which one LOS is inclined about the z-axis relative to the other LOS) will not affect muon sagitta. This concept is illustrated in Fig. 9, and may be understood intuitively. Assume that a straightness monitor pointing to the IP claims that the chambers are perfectly aligned, although this line is rotated by an angle α about the z-axis. A straight, infinite-momentum muon track originating from the IP at the angle of the LOS will therefore also be fit by the superlayers as a straight line (thus no momentum error is introduced), although it will be seen to be rotated by $-\alpha$ about the z-axis. If the LOS is not pointing toward the IP, a sagitta error can result.

A quantitative analysis, based on an earlier L* derivation, has been performed to ascertain the requirements on pointing the straightness monitor axes at the IP. The situation is illustrated in Fig. 9. Two straightness monitors are considered, one with a vertical LOS pointing at the IP, and another inclined at $ß_0$ to the vertical (the y-intercept of the LOS is assumed to miss the IP (which is defined as the origin) by Δy). The muon from the IP is inclined at $ß_\mu$. First the bending (x) coordinates of the superlayer hits are

calculated for the muon, with the chambers rotated about the y-axis in accordance with the torque angle α between the LOS vectors. The bending coordinate of the inner superlayer (x_A) is defined to be zero. We thus state:

$$x_A \equiv 0 \qquad x_B = L_B \sin\alpha\,(z_B/z'_B) \qquad x_C = L_C \sin\alpha\,(z_C/z'_C)$$

$$L_B = y_B - y_A \qquad L_C = y_C - y_A$$

$$z_B = y_B \tan ß_\mu \qquad z_C = y_C \tan ß_\mu \qquad z'_B = (y_B + \Delta y) \tan ß_0$$

$$x_B = \frac{y_B \tan ß_\mu}{(y_B + \Delta y)\tan ß_0} L_B \sin\alpha \qquad x_C = \frac{y_C \tan ß_\mu}{(y_C + \Delta y)\tan ß_0} L_C \sin\alpha$$

We can then define the sagitta as the offset from a straight line between bottom and top layers, and substitute in the above expressions for x_B & x_C to find the sagitta error.

$$s = x_B - (x_C - x_A)\, L_B/L_C$$

$$s = L_B \frac{\tan ß_\mu \sin\alpha}{\tan ß_0}\left(\frac{y_B}{y_B + \Delta y} - \frac{y_C}{y_C + \Delta y}\right)$$

As can be plainly noted in the above expression, $s \rightarrow 0$ as $\Delta y \rightarrow 0$, and the error is largest at high ß. Since, in general, $\Delta y << y_C , y_B$, we approximate:

$$s = L_B \frac{\tan ß_\mu \sin\alpha}{\tan ß_0} \Delta y \left(\frac{1}{y_B} - \frac{1}{y_C}\right)$$

Assuming a maximum $ß_\mu$; then (from Fig. 9) $ß_\mu \approx ß_0$. Plugging in barrel parameters (y_B = 6.3 m, y_C = 8.7 m, L_B = 2.4 m), we then obtain:

$$s(\text{mm}) \approx 0.1\, \Delta y \sin\alpha$$

For small Δy, we can readily substitute a misalignment angle (between the LOS at $ß_0$ and a line from the outer layer to the IP [distance R]); $\Delta y \approx R\, \Delta\theta/\sin ß_0$. This yields:

$$s(\text{rad}) \approx 0.1 \sin\alpha\, R(\text{mm})\, \Delta ß/\sin ß_0$$

The above relation can be used to balance torque errors against LOS misalignment errors; i.e. it shows that if 3 mr of torque rotation is present, a LOS misalignment of 3 mr to the IP will generate a worst-case sagitta error of 18 μm (at $\theta = 30°$). Endcap parameters should be similar.

Finally, this analysis can be generalized to account for the misalignment between two projective lines-of-sight and the IP, as shown in Fig. 10. The leftmost LOS makes an angle with the vertical (at the IP) of $ß_1$ and misses the IP with a y-intercept of Δy_1. The rightmost LOS makes an angle with the vertical (at the IP) of $ß_2$ and misses the IP with a y-intercept of Δy_2. Following the steps outlined previously, it becomes simple to produce the following complicated expression:

$$s = L_B \sin \alpha \left(\frac{\tan ß_\mu\, y_B - \tan ß_1 \left(y_B + \Delta y_1\right)}{\tan ß_2 \left(y_B + \Delta y_2\right) - \tan ß_1 \left(y_B + \Delta y_1\right)} - \frac{\tan ß_\mu\, y_C - \tan ß_1 \left(y_C + \Delta y_1\right)}{\tan ß_2 \left(y_C + \Delta y_2\right) - \tan ß_1 \left(y_C + \Delta y_1\right)} \right)$$

One can simplify this for the case of small Δy, and hopefully result in a more compact expression, but I'll leave this as an exercise for the reader.

One way to look at global alignment of the muon system to the IP is to consider all of the global quantities quoted in this report to be relative to the straightness LOS. The entire global alignment problem then becomes the need to point the straightness monitors at the IP.

7) Summary

Tables 1 - 4 show a summary of the tolerances calculated in this report. Tables 1 & 3 show the requirements for the structure. The width of the smear processes (scattering in the calorimeter and the interaction diamond length) have been divided by a factor 4 (such that the alignment accuracy would be negligible in a quadrature sum). The multiple scattering is taken at 50 GeV, which will probably represent the maximum desired trigger threshold. Table 1 & 2 show values at each θ extreme covered by the detector component, separated by a "|" character (30°| 90° for the barrel; 10°| 30° for the endcap). Tables 3 & 4 list the smallest of these values over the barrel or endcap θ range. An undefined tolerance (i.e. a quantity in a column that has no dependence on a coordinate specified in the row) is labeled with "∞", while an undefined smear (i.e. uncertainty projected along the y axis due to a smear along z) is labeled with "x".

The rightmost column of these tables shows the final tolerances for superlayer alignment; again, Tables 1/3 give the allowance to which the structure must be constructed, and Tables 2/4 give the measurements needed for position correction. This column consists of the most exacting requirement, or the largest smear contribution (if this surpasses the smallest requirement), taken across each row. The "Ultimate Detector Resolution" column of Tables 2/4 shows the (unscaled) prediction of the best detector resolution, as taken from Figs. 7 & 8. This column is not used in assigning the "summary" resolution column; it is presented only for comparison.

One can see that much of the structural requirement is driven by the limited dynamic range of the straightness monitors. If this range could be extended by a factor of 2 to 3, the constraints on the structure could be loosened in many cases to 2-6 mm. In all cases, the dependence on the z-coordinate is fairly loose. This is due to the large interaction diamond, coarse detector resolution, and irrelevance to the momentum measurement in this coordinate. Since there is no quoted range on the local $z_{b,c}$ tolerances for the momentum measurement (Table 2), such limits have been taken from the dynamic range of the straightness monitor system (Table 1). Since none of the drivers considered for structural alignment have any bearing on θ or ϕ, no tolerance is given for them in the summary of Table 1. In reality, some limits are necessary, particularly on θ, which has considerable effect on detector rate (at small angle) and bending/B_field projection.

In some cases (i.e. global alignment of the endcaps), the required structural alignment is more precise than the need arising from precision measurement. This is driven by the trigger assumptions, which prefer a projective geometry (as the trigger requirements are derived in a very approximate fashion here, these quantities should be investigated further). The 200 μm enhanced-resolution requirement for x_G alignment is presented as a goal in these tables, and has not been propagated into the "Summary" column.

8) References

1) Rosenson, L. (MIT), data generated winter/spring (1992).

2) Duinker, P., et. al., "Some Methods for Testing and Optimizing Proportional Wire Chambers", NIM A273 (1988), pg. 814-819.

	Intrinsic Smears (÷4)		Structural Accuracy		
All ±mm and ±mr	Interaction Diamond (7 cm)	Scattering in Calorimeter (50 GeV)	Dynamic Range of Local Alignment	Trigger Roads (10% Loss)	*Summary*
90° | 30°	÷4	÷4			
Barrel					
Δx(b)			1 | 1	2 | 2	1 | 1
Δx(c)			1 | 1	3.25 | 3.25	1 | 1
Δz(b)			1 | 1	3.25 | 3.25	1 | 1
Δz(c)			2 | 2	4.5 | 4.5	2 | 2
Δy(b)			1 | 0.9	∞ | 1.9	1 | 0.9
Δy(c)			1 | 1	∞ | 2.6	1 | 1
ΔX(g)		2 | 2		6.3 | 6.3	6.3 | 6.3
ΔY(g)	x | 6.8	2 | 2		15 | 2.5	15 | 6.8
ΔZ(g)	12 | 12	x | 4		4.5 | 4.5	12 | 12
Δθ	x | 0.35	0.5 | 0.5			
Δϕ		0.5 | 0.5			
30° | 10°					
Endcap					
Δx(b)			1 | 1	2 | 2	1 | 1
Δx(c)			2 | 2	3.25 | 3.25	2 | 2
Δy(b)			1 | 1	1.75 | 1.75	1 | 1
Δy(c)			2 | 2	3.5 | 3.5	2 | 2
Δz(b)			1.7 | 5.7	3 | 10	1.7 | 5.7
Δz(c)			3.4 | 10.4	6 | 20	3.4 | 10.4
ΔX(g)		3.3 | 3.3		5.6 | 5.6	5.6 | 5.6
ΔY(g)	6.8 | 2.1	3.8 | 3.3		4.8 | 4.8	6.8 | 4.8
ΔZ(g)	12 | 12	1.8 | 6.3		4.1 | 14	12 | 12
Δθ	0.35 | 0.13	0.5 | 0.5			
Δϕ		0.5 | 0.5			

Table 1: Alignment factors impacting structural accuracy

			Precision Requirements			
All ±mm and ±mr	Scattering in Calorimeter (500GeV)	Ultimate Detector Resolution	Precision Momentum	Momentum Vector	Mass Resolution	*Summary*
90° | 30°	÷4					
Barrel						
Δx(b)			0.025 | 0.025			0.025 | 0.025
Δx(c)			0.05 | 0.05			0.05 | 0.05
Δz(b)						(1 | 1)
Δz(c)						(2 | 2)
Δy(b)			0.063 | 0.063			0.063 | 0.063
Δy(c)			0.125 | 0.125			0.125 | 0.125
ΔX(g)	0.2 | 0.2	0.33 0.33	0.2 | 0.2 (Goal!)		4.7 | 9.4	4.7 | 9.4
ΔY(g)	0.2 | 0.2	x | 1.6		∞ | 60	∞ | 11	∞ | 11
ΔZ(g)	x | 0.4	13 | 13		∞ | 100	4.7 | 19	4.7 | 19
Δθ	0.05 | 0.05	2.7 | 0.67		∞ | 6.7	1.2 | 1.2	1.2 | 1.2
Δϕ	0.05 | 0.05	0.13 | 0.13			1.2 | 1.2	1.2 | 1.2
30° | 10°						
Endcap						
Δx(b)			0.025 | 0.025			0.025 | 0.025
Δx(c)			0.05 | 0.05			0.05 | 0.05
Δy(b)						(1 | 1)
Δy(c)						(2 | 2)
Δz(b)			0.125 | 0.360			0.125 | 0.360
Δz(c)			0.25 | 0.72			0.25 | 0.72
ΔX(g)	0.33 | 0.33	0.33 | 0.13	0.2 | 0.2 (Goal!)		9.4 | 7.2	9.4 | 7.2
ΔY(g)	0.38 | 0.33	9 | 9		60 | 20	11 | 8.4	11 | 8.4
ΔZ(g)	0.18 | 0.63	15 | 53		100 | 100	19 | 48	19 | 48
Δθ	0.05 | 0.05	2.7 | 2.7		6.7 | 2.9	1.2 | 1.2	1.2 | 1.2
Δϕ	0.05 | 0.05	1.3 | 1.3			1.2 | 1.2	1.2 | 1.2

Table 2: Alignment factors impacting Precision Measurements

	Intrinsic Smears (÷4)		Structural Accuracy		
All ± mm and ± mr	Interaction Diamond (7 cm)	Scattering in Calorimeter (50 GeV)	Dynamic Range of Local Alignment	Trigger Roads (10% Loss)	*Summary*
	÷4	÷4			
Barrel					
Δx(b)			1	2	1
Δx(c)			1	3.25	1
Δz(b)			1	3.25	1
Δz(c)			2	4.5	2
Δy(b)			1	1.9	1
Δy(c)			1	2.6	1
ΔX(g)		2		6.3	6.3
ΔY(g)	6.8	2		2.5	6.8
ΔZ(g)	12	4		4.5	12
Δθ	0.35	0.5			
Δϕ		0.5			
Endcap					
Δx(b)			1	2	1
Δx(c)			2	3.25	2
Δy(b)			1	1.75	1
Δy(c)			2	3.5	2
Δz(b)			1.7	3	1.7
Δz(c)			3.4	6	3.4
ΔX(g)		3.3		5.6	5.6
ΔY(g)	2.1	3.3		4.1	4.1
ΔZ(g)	12	6.3		4.4	12
Δθ	0.13	0.5			
Δϕ		0.5			

Table 3: Most Restrictive Alignment Factors (Structural Accuracy)

			Precision Requirements			
All ±mm and ±mr	Scattering in Calorimeter (500 GeV)	Ultimate Detector Resolution	Precision Momentum	Momentum Vector	Mass Resolution	*Summary*
	÷4					
Barrel						
Δx(b)			0.025			0.025
Δx(c)			0.05			0.05
Δz(b)						1
Δz(c)						2
Δy(b)			0.063			0.063
Δy(c)			0.125			0.125
ΔX(g)	0.2	0.33	0.2 (Goal!)		4.7	4.7
ΔY(g)	0.2	1.6		60	11	11
ΔZ(g)	0.4	13		100	4.7	4.7
Δθ	0.05	2.7		6.7	1.2	1.2
Δϕ	0.05	0.13			1.2	1.2
Endcap						
Δx(b)			0.025			0.025
Δx(c)			0.05			0.05
Δy(b)						1
Δy(c)						2
Δz(b)			0.125			0.125
Δz(c)			0.25			0.25
ΔX(g)	0.33	0.13	0.2 (Goal!)		7.2	7.2
ΔY(g)	0.33	9		20	8.4	8.4
ΔZ(g)	0.63	15		100	19	19
Δθ	0.05	2.7		2.9	1.2	1.2
Δϕ	0.05	1.3			1.2	1.2

Table 4: Most Restrictive Alignment Factors (Precision Measurement)

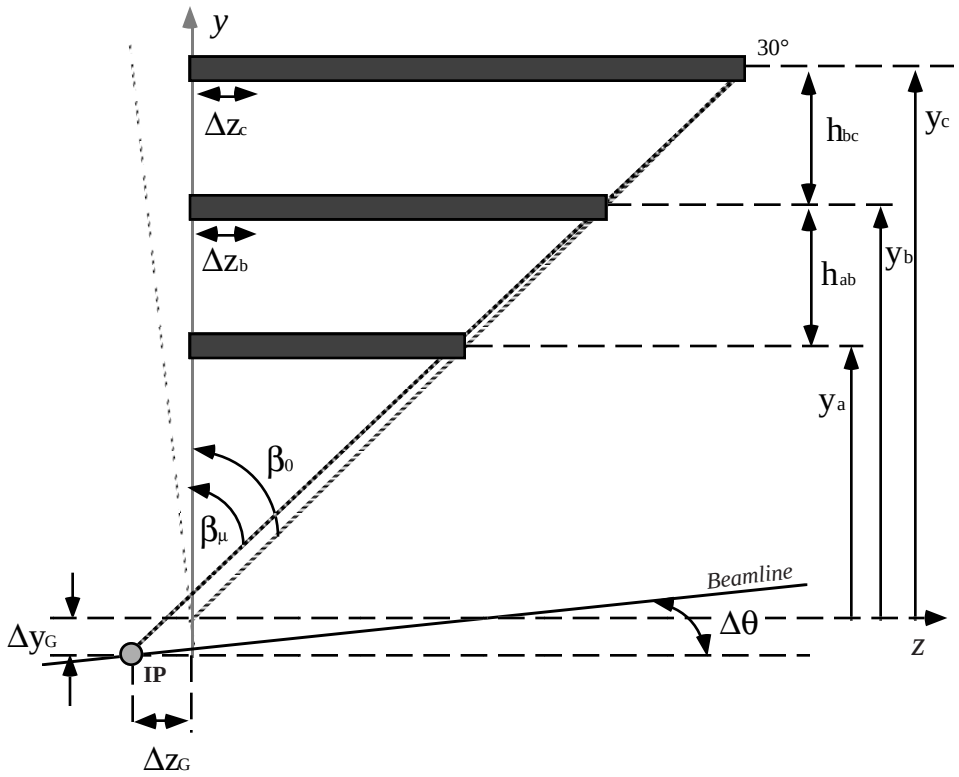

Figure 1: Barrel Requirements Definition; rθ

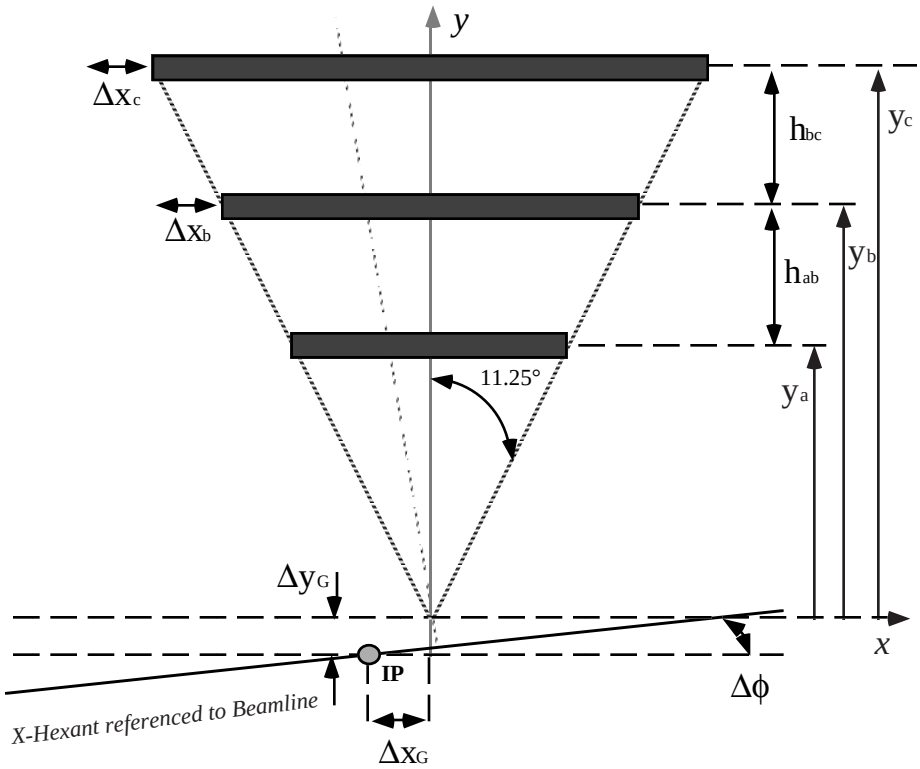

Figure 2: Barrel Requirements Definition; rϕ

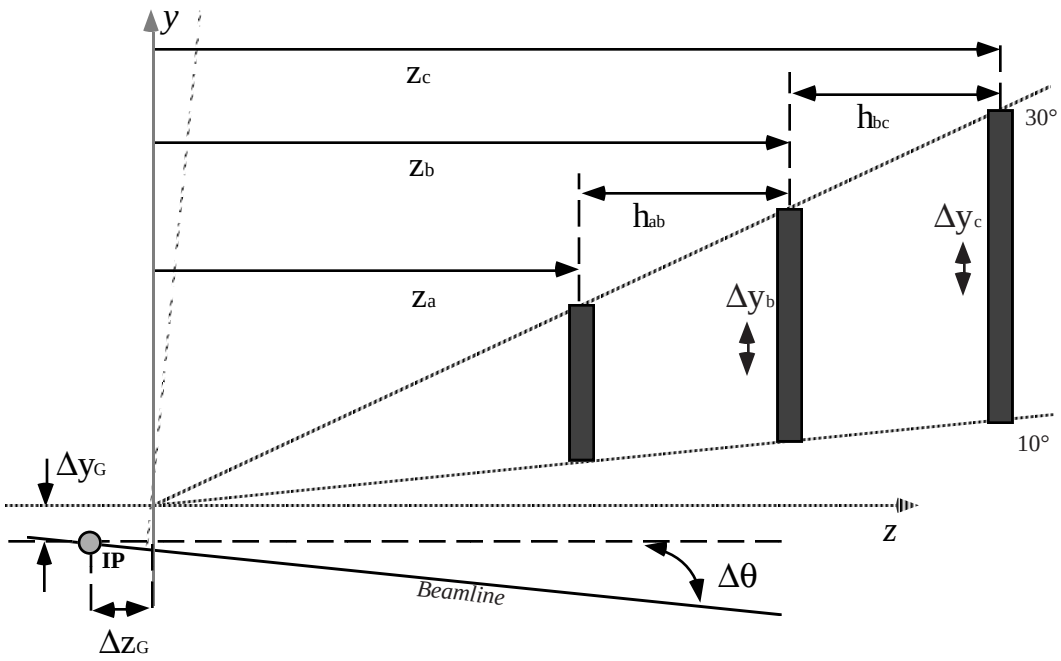

Figure 3: Endcap Requirements Definition; rθ

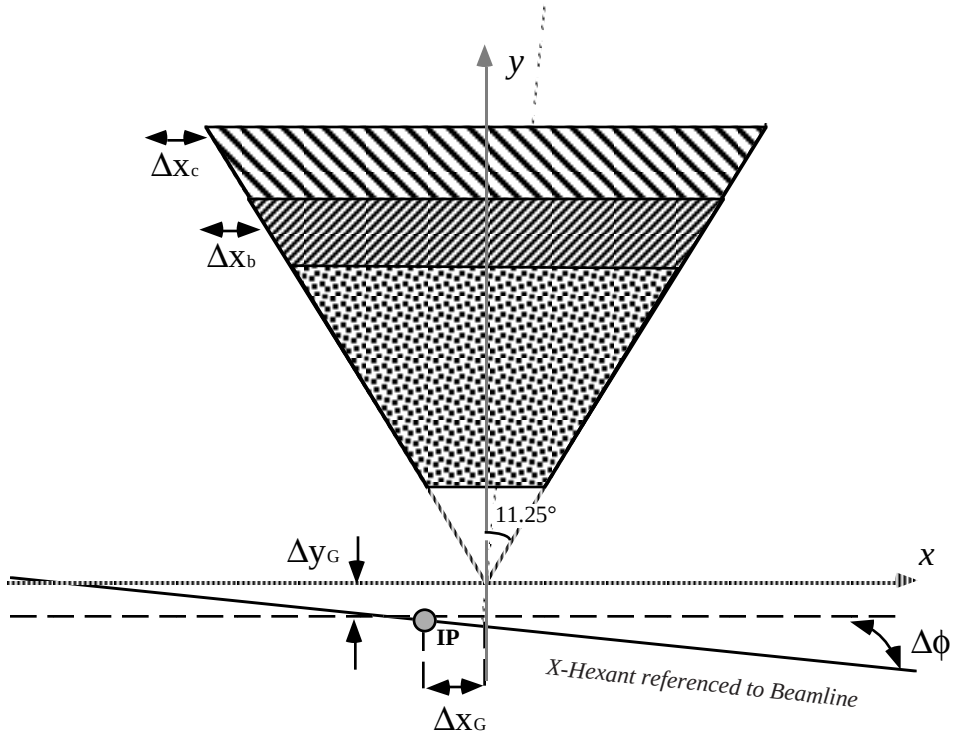

Figure 4: Endcap Requirements Definition; rϕ

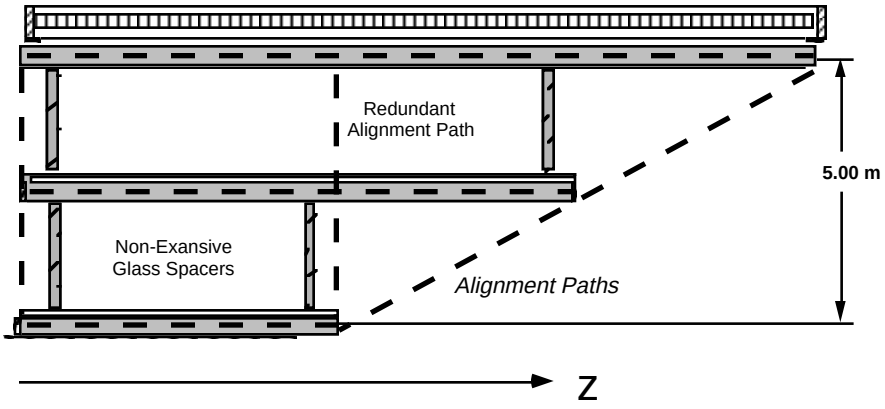

a) $r\theta$ View

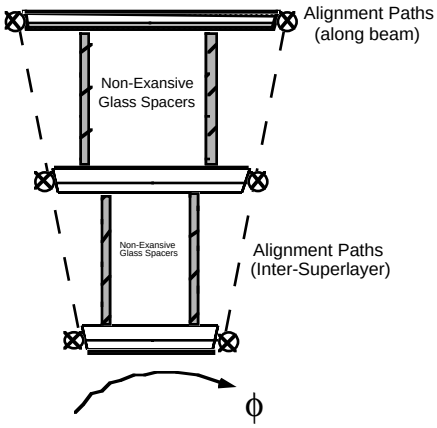

b) $r\phi$ View

Figure 5: Possible scheme for aligning muon barrel

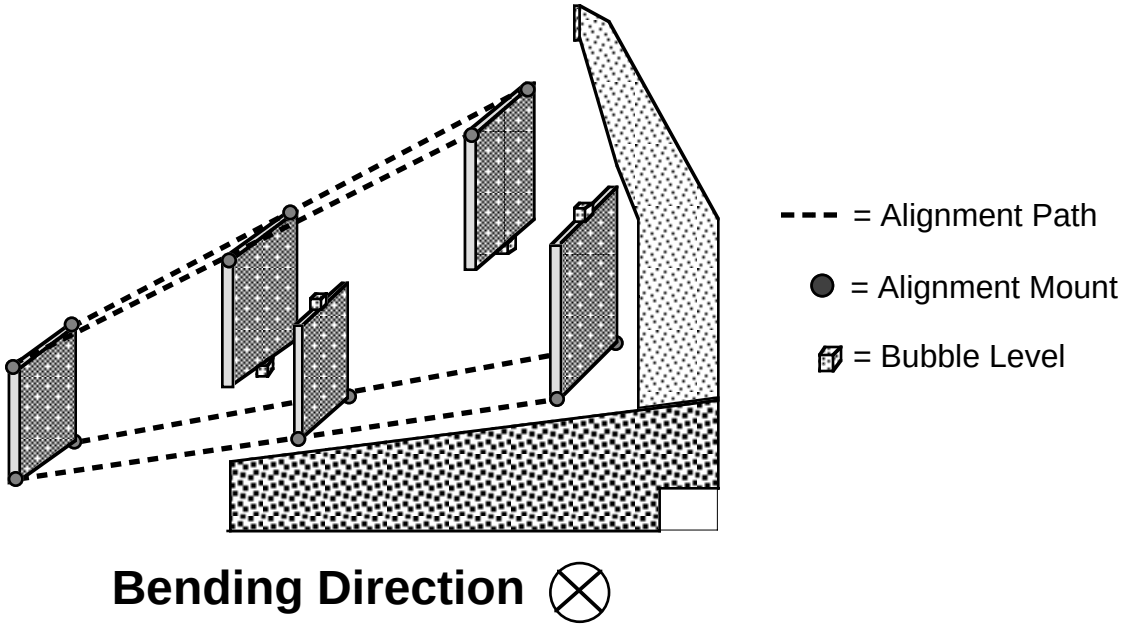

Figure 6: Possible scheme for aligning muon endcap

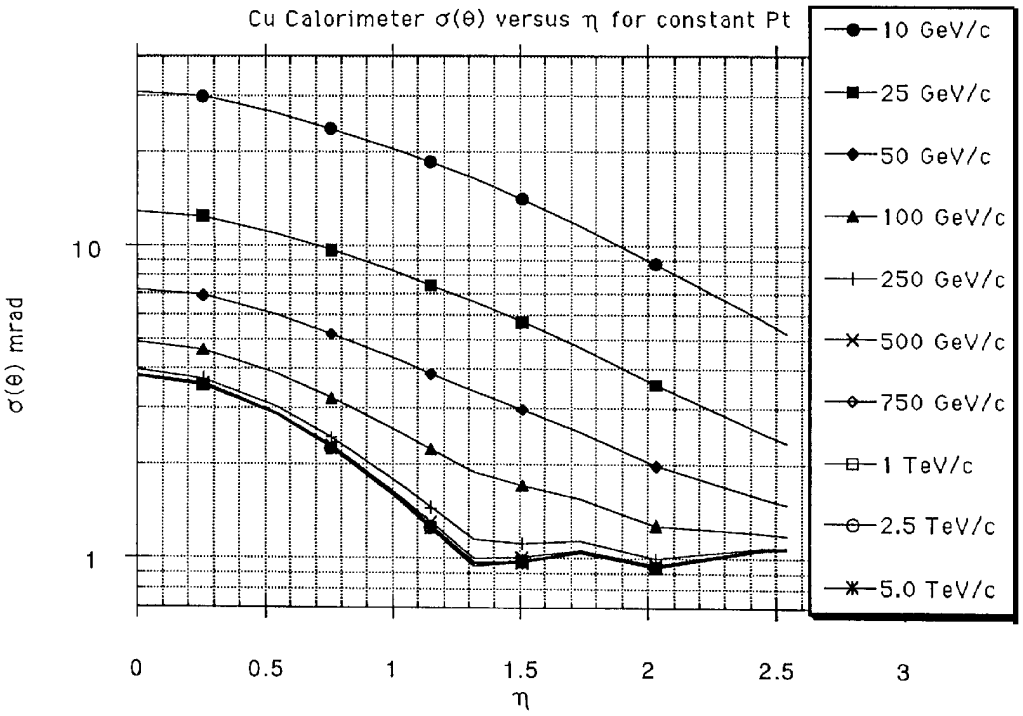

Figure 7a: θ resolution in muon detector

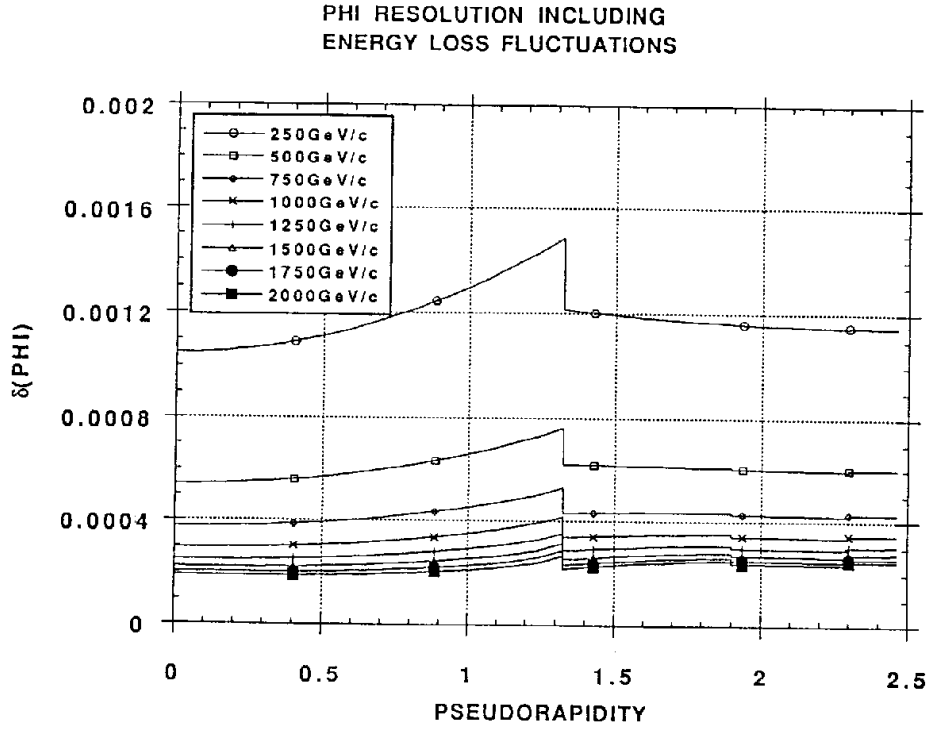

Figure 7b: ϕ resolution in muon detector

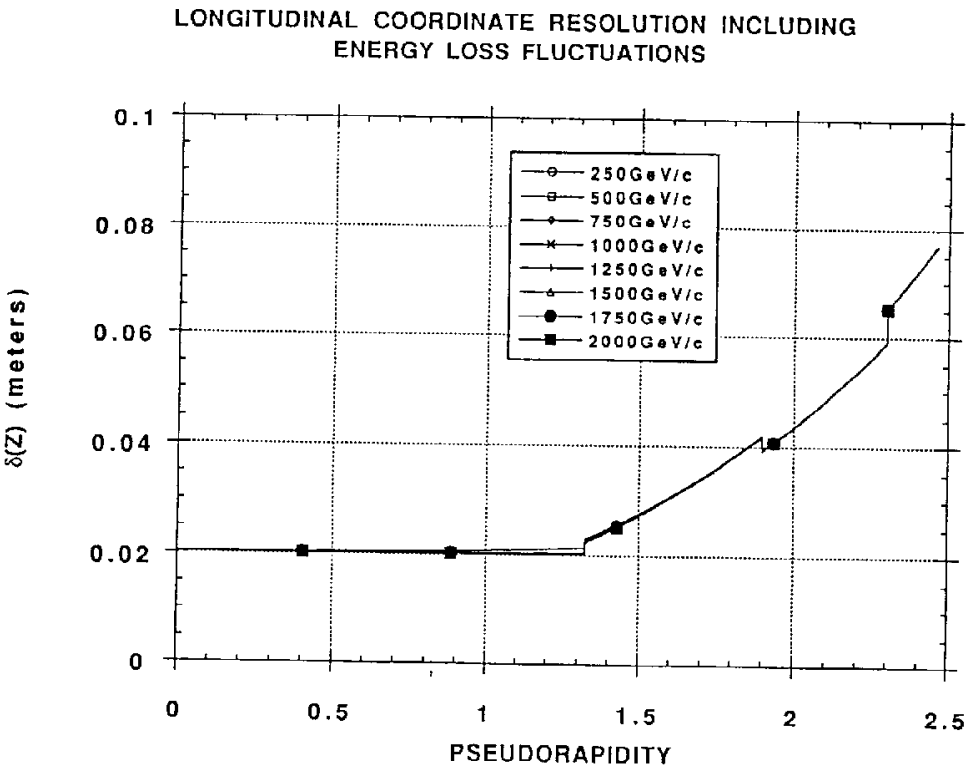

Figure 8a: z resolution in muon detector

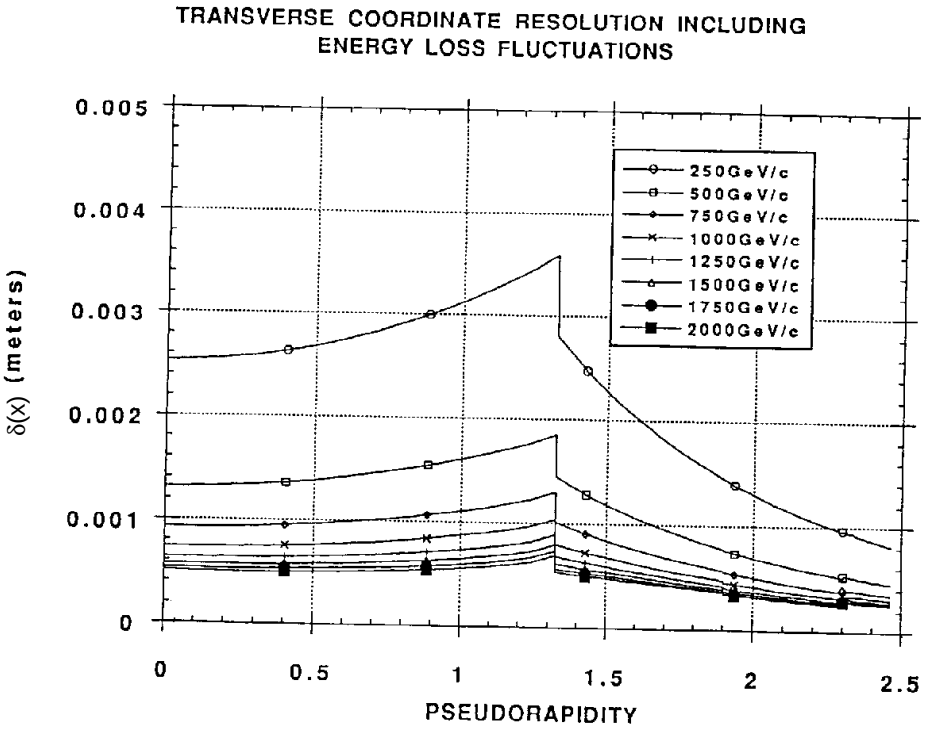

Figure 8b: x resolution in muon detector

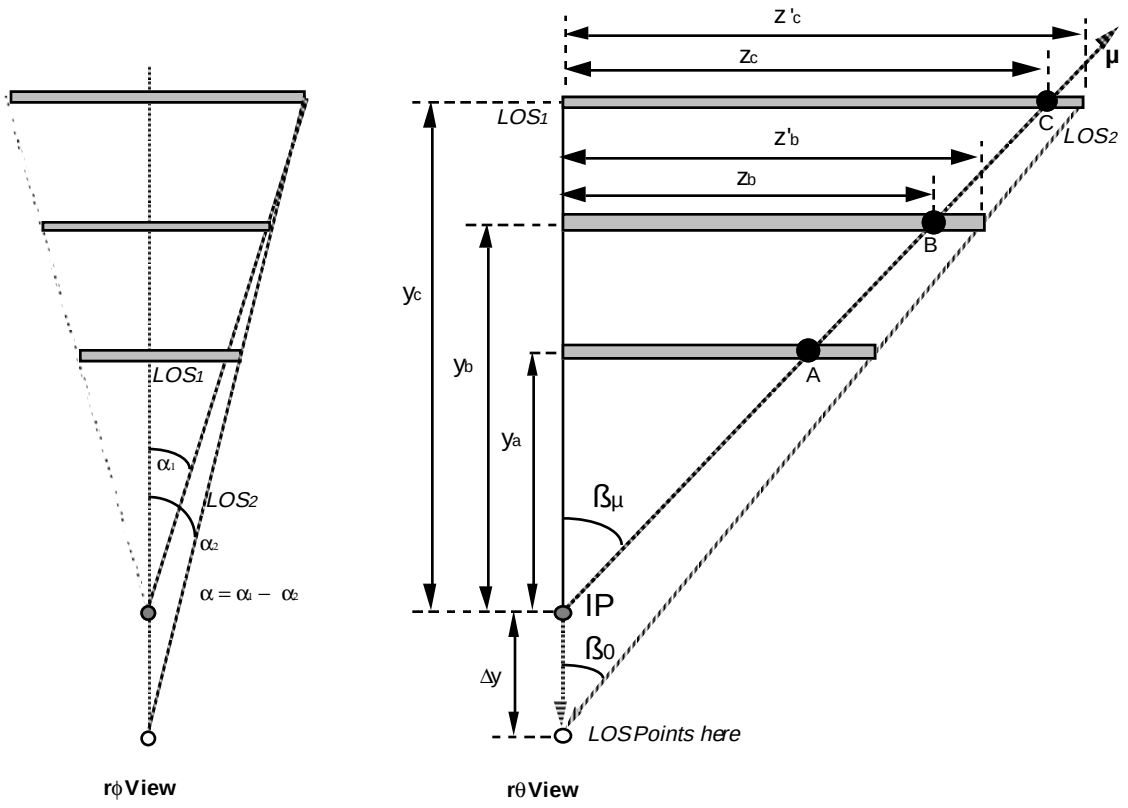

Figure 9: Analysis of sagitta error from superlayer torque

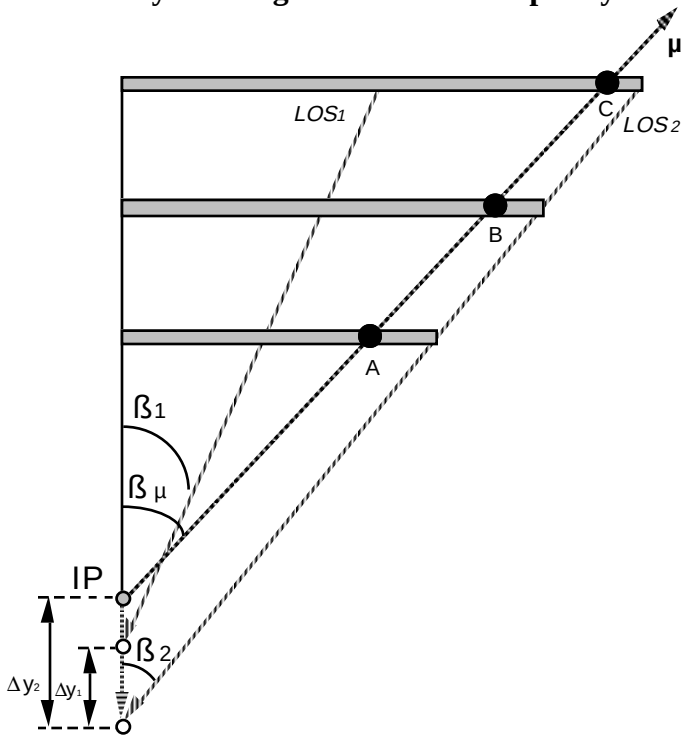

Figure 10: General analysis of sagitta error from superlayer torque